

K^+ mesons as a probe of the nuclear interior

W. R. Coker, J. D. Lumpe, and L. Ray

Department of Physics, The University of Texas at Austin, Austin, Texas 78712

(Received 15 November 1984)

The sensitivity of intermediate energy K^+ meson-induced elastic and inelastic differential cross section predictions to nuclear structure effects in the nuclear interior is examined for ^{40}Ca and ^{208}Pb targets. The observed sensitivity for K^+ mesons is compared to that obtained with intermediate energy protons. In general, the K^+ meson + nucleus elastic and inelastic scattering differential cross sections are an order of magnitude more sensitive to details of nucleon density distributions in the nuclear interior than corresponding proton-nucleus cross sections at comparable incident momentum. It is found that theoretical analyses of high quality K^+ meson + nucleus data which extend to 3 fm^{-1} momentum transfer could, in principle, provide new information regarding neutron ground state and transition density distributions in the interiors of large nuclei.

I. INTRODUCTION

Studies of the structure of atomic nuclei by way of electromagnetic and hadronic probes have been actively pursued for over 40 years. During this time a great deal of reliable information regarding ground state densities, transition densities, single particle wave functions, etc., has been compiled in the literature. Accurate determinations of nuclear charge distributions have been provided through combined model-independent analyses of high momentum transfer elastic and inelastic electron scattering differential cross section data¹⁻⁶ together with muonic atom data.⁶ These results have imposed severe constraints on nuclear structure models^{1,2} and have possibly provided information about three-body forces and meson exchange currents in nuclei.⁷ Analyses of intermediate energy proton,⁸ pion,^{9,10} and alpha particle scattering data¹¹ have in some cases yielded fairly accurate information for neutron transition densities, and also for the *relative* differences between neutron ground state density distributions of neighboring nuclei in the surface and tail regions of the distribution. Determination of *absolute* neutron densities in the surface region through analysis of strong interaction projectile scattering data turns out to be very difficult, because of the large and varied contributions to the hadron-nucleus scattering observables arising from alternate treatments of medium effects,¹² target nucleon correlations,^{8,13} spin dependence of the hadron-nucleon interaction,⁸ and relativistic dynamics.¹⁴ Attempts at careful examination of the behavior of the neutron ground state and transition densities in the nuclear interior have also been unsuccessful, owing to the very large absorption experienced by the available intermediate energy hadrons: protons, pions, and alpha particles.⁸⁻¹¹

Consideration of the K^+ meson as a probe of the nuclear interior has been a topic of interest in recent years,¹⁵⁻²¹ due to the fact that the K^+ meson + nucleon (K^+N) effective interaction strength, as characterized by the total cross section, is relatively weak. The K^+N total cross sections vary between 10 and 20 mb for incident momenta below $1\text{ GeV}/c$ (Ref. 15) compared to ~ 40 mb for

protons and ~ 50 – 100 mb for pions in this same momentum range.²² It is thus expected that K^+ mesons will have a significantly longer mean free path in nuclear matter than protons, alpha particles, or pions at comparable energies. Furthermore, contributions to the K^+ meson + nucleus (K^+A) observables arising from multiple scattering of the K^+ meson from individual target nucleons¹³ should be reduced in importance compared to that for other hadrons, thus simplifying the demands on the theoretical model. Finally, K^+ mesons are spinless, eliminating problems such as those found in proper treatments of the interaction between two nucleons in the description of proton-nucleus scattering.¹⁴ Consequently, analyses of K^+A scattering data should provide greater sensitivity to structure details in the nuclear interior and possibly more accurate, absolute neutron density information than has been obtained from other available hadronic probes.

In this work, a quantitative comparison between the sensitivities of K^+A and proton-nucleus (pA) elastic and inelastic scattering differential cross sections to perturbations in the neutron ground state and transition densities is provided. These results are used to specify the type and quality of K^+A data needed in analyses aimed at deducing new and meaningful nuclear structure information.

In Sec. II the theoretical model used in this analysis is briefly outlined. The relative sensitivity of K^+A and pA elastic and inelastic scattering cross sections to the ground state and transition matter densities is discussed in Secs. III and IV, respectively. A summary and conclusions are given in Sec. V.

II. THEORETICAL MODEL

The nonrelativistic multiple scattering optical potential formalism of Kerman, McManus, and Thaler (KMT) (Ref. 13) forms the theoretical basis for the analysis presented here. In this approach the t matrix for elastic hadron-nucleus scattering, T_{00} , is expressed in terms of the optical potential according to

$$T_{00} = \frac{A}{(A-1)} T'_{00}, \quad (1a)$$

where

$$T'_{00} = U^{\text{opt}} + U^{\text{opt}} P G P T'_{00} \quad (1b)$$

and

$$G = (E^{(+)} - K - H_A + i\epsilon)^{-1}. \quad (1c)$$

Here A is the number of target nucleons, G is the projectile-nucleus many-body propagator, P projects the ground state of the target nucleus, $E^{(+)}$ is the projectile energy in the projectile-nucleus center-of-momentum (c.m.) system, K is the kinetic energy operator, and H_A is the full nuclear Hamiltonian. The optical potential for elastic scattering is given by

$$U^{\text{opt}} = U_{00} + \sum_{\alpha \neq 0} U_{0\alpha} \frac{1}{E^{(+)} - \epsilon_\alpha - K - U_{\alpha\alpha}} U_{\alpha 0}, \quad (2)$$

where ϵ_α is the excitation energy of the intermediate nuclear excited state α with wave function $|\phi_\alpha\rangle$ ($|\phi_0\rangle$ denotes the nuclear ground state), and the effective interaction matrix elements, $U_{\alpha\beta}$, are given by

$$U_{\alpha\beta} = (A-1) \langle \phi_\beta | \tau | \phi_\alpha \rangle. \quad (3)$$

In Eq. (3), τ is the effective projectile-target nucleon interaction operator given by

$$\tau = v + v G \hat{A} \tau, \quad (4)$$

where v is an isospin averaged projectile-target nucleon interaction potential and the antisymmetrization operator, \hat{A} , allows only physical states of the target nucleus as intermediate scattering states.

Experience with intermediate energy proton-nucleus optical potentials indicates that the free proton-nucleon (pN) scattering t matrix provides an accurate approximation for τ (Ref. 8). This so-called "impulse approximation" (IA), (Ref. 13) together with local, first-order optical potentials [i.e., those in which the second term in Eq. (2) is neglected] provide fairly good descriptions of pA elastic scattering differential cross section data for the cases considered here.^{23,24}

The K^+N scattering t matrix is characterized by a smooth and gentle variation with energy and momentum transfer;^{22,25-27} no resonance structure appears, unlike the case for pions^{9,10} and K^- (Ref. 15). This feature implies that nonlocality and off-shell effects should be minimal in K^+A reactions as well.²¹ In addition, the relative weakness of the K^+N interaction results in a further reduction of second-order optical potential effects.¹⁷ Furthermore, there is no true absorption mechanism¹⁵ associated with

$$\left\{ \frac{d^2}{dr^2} - \frac{l(l+1)}{r^2} - \frac{2\mu\epsilon^2}{(\hbar c)^2} [U^{\text{opt}}(r) + U_{\text{Coul}}(r)] + k_N^2 \right\} \psi_{lj}(r) = 0, \quad (9)$$

where $\mu\epsilon^2 = E_p E_T / (E_p + E_T)$, E_T is the target nucleus total relativistic energy in the projectile-target c.m. system, k_N is the projectile-target c.m. wave number, and $U_{\text{Coul}}(r)$ is the Coulomb potential. The elastic scattering

K^+A scattering, unlike the situation in the pion-nucleus system,^{9,10} Because of this, local, first-order optical potentials are adequate for the description of K^+A scattering, at least in the context of the sensitivity study carried out here.

For the pA and K^+A calculations, the optical potential in momentum space is approximated as

$$\tilde{U}^{\text{opt}}(\mathbf{k}, \mathbf{k}') \simeq (A-1) t(\mathbf{q}) \tilde{\rho}(\mathbf{q}), \quad (5)$$

where $t(\mathbf{q})$ is the on-shell, free projectile-target nucleon t matrix, $\tilde{\rho}(\mathbf{q})$ is the one-body target density form factor, and $\mathbf{q} = \mathbf{k} - \mathbf{k}'$ is the momentum transfer. According to nonrelativistic multiple scattering theory¹³ the projectile-target nucleon t matrix in Eq. (5) must be evaluated in the projectile-nucleus c.m. system. This can be achieved by exploiting the Møller relation for invariant t matrices, given by¹³

$$t(\mathbf{q}) = \frac{\epsilon_p \epsilon_N}{E_p E_{SN}} t_{\text{two-body}}(\mathbf{q}). \quad (6)$$

In this expression $t_{\text{two-body}}(\mathbf{q})$ represents the projectile-target nucleon t matrix in the projectile-nucleon c.m. frame; $\epsilon_p(\epsilon_N)$ and $E_p(E_{SN})$ are the projectile (target nucleon) total relativistic energies in the projectile-nucleon and projectile-nucleus c.m. systems, respectively. The two-body t matrix is related to the two-body scattering amplitude, $F(\mathbf{q})$ [e.g., $F(\mathbf{q}) = f(\mathbf{q}) + g(\mathbf{q}) \sigma \cdot \hat{\mathbf{n}}$ for the K^+N system], by the prescription,^{8,13,28}

$$t_{\text{two-body}}(\mathbf{q}) = -2\pi(\hbar c)^2 [(\epsilon_p + \epsilon_N) / (\epsilon_p \epsilon_N)] \times F(\mathbf{q}). \quad (7)$$

The explicit K^+A nonrelativistic optical potential is obtained by combining the above expressions for $t(\mathbf{q})$ and summing over target nucleon spins. In coordinate space the local K^+A optical potential therefore becomes^{8,13,29}

$$U^{\text{opt}}(r) = - \frac{(A-1)}{A} \frac{(\hbar c)^2 (\epsilon_K + \epsilon_N)}{\pi E_K E_{SN}} \times \sum_{i=p,n} \int_0^\infty dq q^2 j_0(qr) f_i(q) \tilde{\rho}_i(q), \quad (8)$$

where ϵ_K and E_K are the kaon total relativistic energies in the K^+N and K^+A c.m. systems, respectively, i denotes target neutrons or protons, and $f_i(q)$ is the spin-independent K^+N scattering amplitude. The first-order, spin-dependent pA optical potential is given in Refs. 8, 13, and 24. Both the K^+A and pA elastic scattering observables are obtained by solving the Schrödinger equation with relativistic kinematics (RSE) and the above K^+A and pA optical potentials. The radial part is given by^{8,24}

observables are obtained by the usual asymptotic matching conditions.

The K^+N scattering amplitudes were generated using the $l=0, 1$, and 2 phase shifts of Martin²⁵ and typical

tabulated phase shift values for the small, higher partial waves through $l=4$ (Refs. 22, 26, and 27). The *SP82* energy independent nucleon-nucleon (NN) phase shift solution of Arndt *et al.*²² provided the pN scattering amplitudes.

The proton densities for ^{40}Ca and ^{208}Pb were obtained from the model-independent charge densities of Refs. 3 and 4, respectively, by unfolding the single proton charge form factor and correcting for contributions to the charge density arising from the electric form factor of the neutron and nucleon magnetic moments.^{8,30} The various forms assumed for the ground state neutron densities are given below and in Sec. III.

The inelastic transition angular distributions were calculated using the distorted-wave Born approximation (DWBA) formalism³¹ with collective model transition potentials (see Sec. IV). These calculations were performed using a modified version of the DWBA code VENUS.³² Deformed spin-orbit coupling was included in the (p,p') calculations.³³

The KMT-IA model discussed above was applied to 442 MeV $\text{K}^+ + ^{40}\text{Ca}$ elastic scattering; the comparison with data,²⁰ shown in Fig. 1, is fair. The calculated angular distribution is about 40% and 20% low at the first minimum and maximum, respectively. The ^{40}Ca neutron density assumed in this calculation was

$$\rho_n(r) |_{\text{theory}} = \rho_p(r) |_{(e,e)} + [\rho_n(r) - \rho_p(r)]_{\text{DME}}, \quad (10)$$

where $\rho_p(r) |_{(e,e)}$ is the experimental proton density and

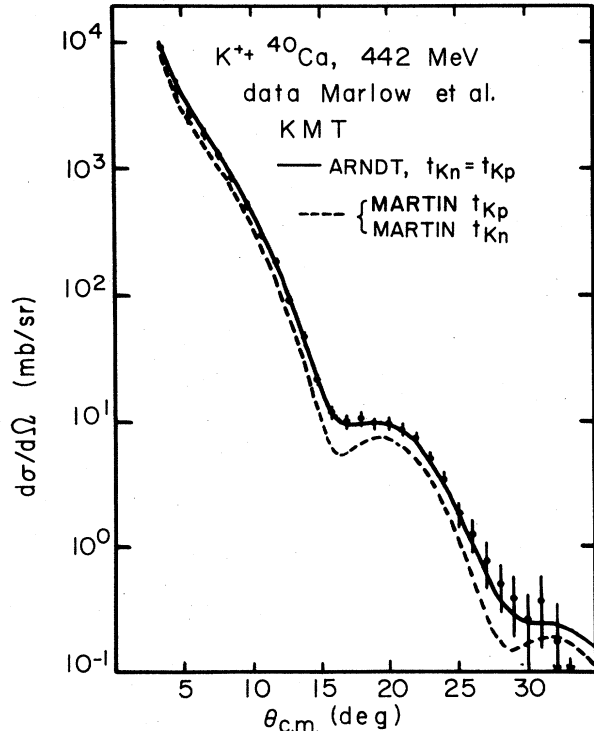


FIG. 1. First-order KMT-IA predictions compared with elastic differential cross section data for 442 MeV $\text{K}^+ + ^{40}\text{Ca}$. The dashed curve corresponds to Martin K^+N amplitudes whereas $t_{\text{K}^+\text{n}} = t_{\text{K}^+\text{p}}$ (Arndt, solution CMK) is assumed in obtaining the solid curve.

the quantities in square brackets correspond to the density matrix expansion (DME) densities of Ref. 34.

It is customary in meson-nucleus physics to solve an approximate form of the Klein-Gordon equation (KGE) (Refs. 9 and 10) to generate meson-nucleus observables. It is appropriate therefore to compare our KMT-IA results with corresponding predictions based on the KGE. Two qualifying remarks need to be made before discussing these comparisons. First, most practical applications of the KGE involve two approximations. These approximations are the following: (1) terms involving the nuclear potential squared are omitted and (2) the asymptotic wave functions are matched to nonrelativistic Coulomb wave functions. These approximations result in a radial KGE which, in fact, has the same form as the radial Schrödinger equation, Eq. (9), except that $\mu_\epsilon c^2$ is replaced by E_K . The appearance of E_K rather than $\mu_\epsilon c^2$ in the radial KGE follows directly from the use of a relativistic equation of motion which is, necessarily, a one-body equation for the projectile. The KGE fails to account for the recoil of the target nucleus. Since $E_K > \mu_\epsilon c^2$ the differential cross section predictions for the KGE are larger in magnitude than those of the RSE, even when identical optical potentials are used. For 442 MeV $\text{K}^+ + ^{40}\text{Ca}$ elastic scattering this increase is 17% at the first minimum at 17° c.m. The shapes of the KGE and RSE predictions are essentially the same. The second remark concerns the form of the optical potential. In most meson-nucleus scattering models the Kisslinger off-shell form is assumed for the $l=1$ meson-nucleon partial wave amplitude.^{9,10} Since the $l=1$ K^+N phase shifts do not dominate the full K^+N amplitudes,^{22,25-27} the local, KMT optical potential calculations agree very well with nonlocal, Kisslinger optical potential results²¹ when the same K^+N phase shifts and nuclear densities are used. The results in Fig. 1 are also in reasonable agreement with the momentum space, KGE predictions obtained by Marlow *et al.*,²⁰ which use slightly different nuclear densities. Finally, it is worth noting that many formulations^{15,16} of the meson-nucleus optical potential given in the literature and widely used for pion and kaon elastic scattering cross section calculations are inconsistent with Eqs. (6)–(8), failing to distinguish, for instance, between meson-nucleon and meson-nucleus frames of reference.

The underestimate of the data beyond 15° obtained with the first-order KMT-IA calculation might be due to inadequate K^+N amplitudes, or the effects of higher-order corrections due to the nuclear medium and target nucleon correlations, or off-shell effects, or to some type of relativistic correction.¹⁴ Because of the current paucity of K^+N data^{15,22,25-27} it would seem likely that an alternate set of K^+N amplitudes could be found which remains consistent with the limited K^+N data, but which results in better agreement between KMT-IA predictions and the data. Using flexible parametrizations, it was found that the forward angle spin-independent K^+N amplitudes [it is this particular K^+N amplitude which governs the K^+A predictions as seen in Eq. (8)] were tightly constrained by the K^+N total cross section measurements and forward angle differential cross section data. No significant improvement in the KMT-IA pre-

dictions of the 442 MeV $K^+ + {}^{40}\text{Ca}$ data was obtained with any of a variety of alternative K^+N amplitudes, consistent with available data. It has also been estimated that second-order correlation contributions are fairly small for this case.¹⁷ Nonlocal optical potential calculations by Siegel, Kaufmann, and Gibbs³⁵ demonstrate that the calculated K^+A cross section at forward angles can be increased sufficiently to fit the data by introducing a cutoff in the off-shell portion of the K^+N t matrix.³⁶ Thus it is not clear at present whether the inadequacy of the KMT-IA model is due to inaccurate K^+N data, off-shell dependencies of the K^+N t matrix, or perhaps some hitherto uninvestigated effect, associated for instance with relativistic dynamics.¹⁴

It is, however, possible to fit these K^+A data using a phenomenological, local folding model. For example, the solid curve in Fig. 1 corresponds to setting $t_{K^+n} = t_{K^+p}$ where the CMK phase shift solution of Arndt²² was used for t_{K^+p} . This calculation agrees with the data at each point; however, in reality $t_{K^+p} \neq t_{K^+n}$, so that the calculation has no microscopic interpretation.

Our primary goal in this work was to investigate the sensitivity to neutron densities over a wide range of momentum transfer. It is important, therefore, to use a realistic K^+N effective interaction, deferring for now any further consideration of the above theoretical questions. It is reasonable to expect that the KMT-IA model will accurately predict the *changes* in the angular distributions resulting from perturbations in the densities, even though the absolute predictions are not perfect. For this reason the K^+N scattering amplitudes of Martin²⁵ are used, despite their possible deficiencies with respect to the predicted K^+A observables, rather than adjusted phenomenological effective interactions which are inconsistent with K^+N data. It is interesting to note however that the sensitivity results discussed below are *not* significantly altered if the calculations are repeated using $t_{K^+n} = t_{K^+p}$ (see Ref. 37).

III. ELASTIC SCATTERING RESULTS

The following cases were considered in this sensitivity study: $K^+ + {}^{40}\text{Ca}$ and ${}^{208}\text{Pb}$ at 442 and 991 MeV; and $p + {}^{40}\text{Ca}$ and ${}^{208}\text{Pb}$ at 297 and 800 MeV. The lower (higher) energy reactions correspond to a c.m. momentum of 3.9 fm^{-1} (7 fm^{-1}). The neutron densities were parametrized as

$$\rho_n(r) = \rho_0 \left[\frac{1}{1 + e^{(r-c)/z}} + A e^{-d(r-r_0)^2} j_0(\omega r) + s_1 e^{-d_1(r-r_1)^2} \right], \quad (11)$$

where c and z were selected (with $A = s_1 = 0$) to most nearly reproduce the theoretical neutron density of Eq. (10) in the surface region. Calculations with $A = s_1 = 0$ provided the standard differential cross sections for each case; the resulting angular distributions are shown in Figs. 2–5.

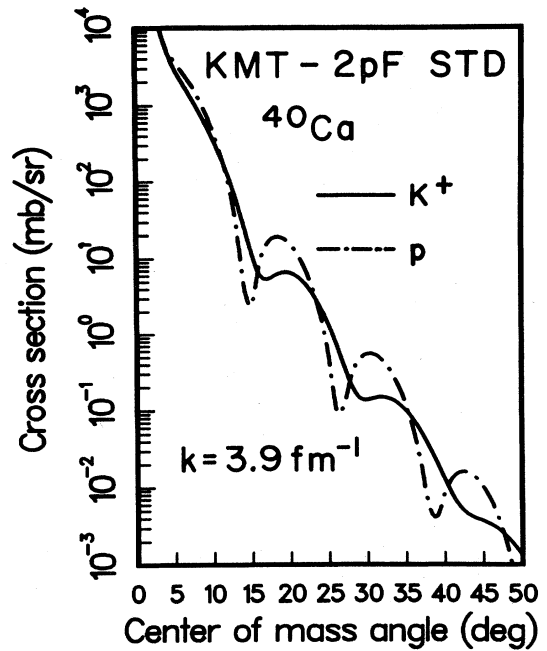


FIG. 2. KMT reference calculations for K^+ (solid curve) and proton (dot-dashed curve) induced elastic scattering from ${}^{40}\text{Ca}$ at the lower energies using the two-parameter Fermi density.

The neutron densities were then varied by adding either a Gaussian bump ($s_1 \neq 0$) in the interior, surface, or tail regions of the neutron density or by adding a damped j_0 ($A \neq 0$) wiggle in the interior. The normalization constant ρ_0 was readjusted in each case. Four such calculations were carried out for both the K^+A and pA reactions, at both energies, for ${}^{40}\text{Ca}$ and ${}^{208}\text{Pb}$. The resulting angular distributions form the basis for our sensitivity study. The

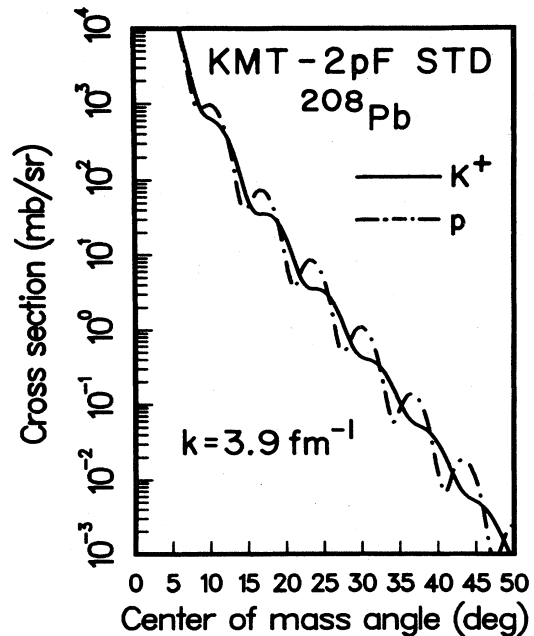


FIG. 3. Same as Fig. 2, except for ${}^{208}\text{Pb}$ at the lower energies.

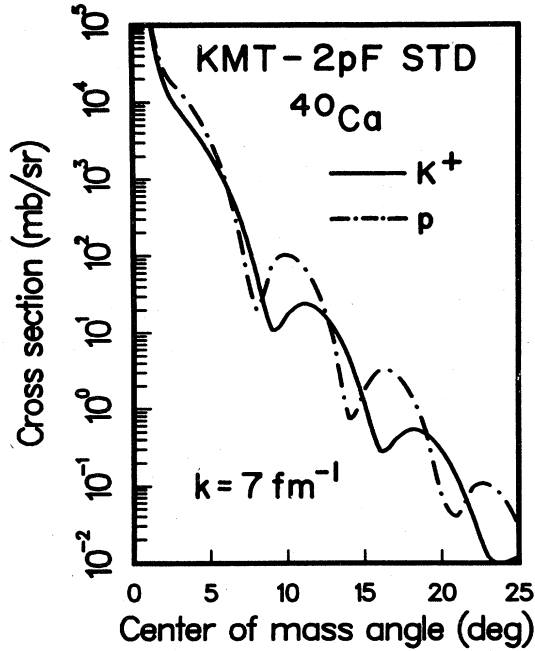


FIG. 4. Same as Fig. 2, except for ^{40}Ca at the higher energies.

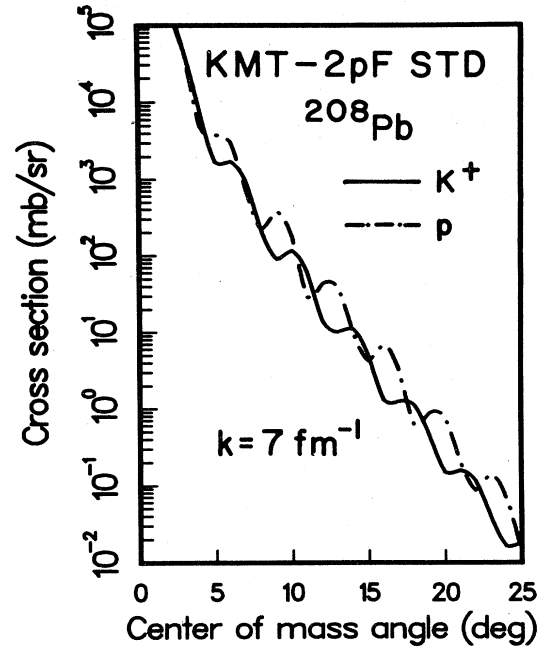


FIG. 5. Same as Fig. 2, except for ^{208}Pb at the higher energies.

values of s_1 and A were fixed at 10% of the unperturbed density at the point of application (except for ^{208}Pb , where a 30% Gaussian bump was applied in the interior). The complete set of parameters describing $\rho_n(r)$ in Eq. (11) used in these calculations is given in Table I. The corresponding neutron densities are shown in Fig. 6. The changes in the interior neutron densities affected by these perturbations were chosen to be comparable in magnitude to the uncertainties in $\rho_n(r)$ deduced in analyses of 800 MeV pA elastic scattering data.^{38,39}

A comparison of the changes in the predicted differential cross sections between the pA and K^+A cases at comparable c.m. momentum can give insight regarding the relative sensitivity of these two probes to the interior, surface, and tail regions of the neutron density. The calculations including $j_0(\omega r)$ provide information concerning sensitivity to a specific Fourier component of the interior

neutron density.

Results of the calculations are presented in Figs. 7–10 in the form $\{[d\sigma(\text{with perturbation}) - d\sigma(\text{no perturbation})]/d\sigma(\text{no perturbation})\} \times 100\%$. The large percentage changes which occur in the pA cases near the diffractive minima (indicated by arrows) are relatively inconsequential and are merely a reflection of the steepness of the pA differential cross sections at these points. It is important to note that these changes near the diffractive minima are very small in magnitude. Little if any nuclear structure information of the type being considered here would be affected by careful theoretical descriptions of the deep diffractive minima in the pA angular distributions. These remarks apply in part to the K^+A cross sections also; however, the K^+A angular distributions tend to be relatively smooth and lack the deep diffractive minima found in the pA angular distributions, because of the rela-

TABLE I. Neutron model density parameters.

Nucleus	Case	c (fm)	z (fm)	A	d_0 (fm ⁻²)	r_0 (fm)	ω (fm ⁻¹)	s_1	d_1 (fm ⁻²)	r_1 (fm)
^{40}Ca	Standard	3.451	0.534	0.0				0.0		
	Interior	3.451	0.534	0.0				0.1	1.0	0.0
	Surface	3.451	0.534	0.0				0.05	1.0	3.451
	Tail	3.451	0.534	0.0				0.01	1.0	4.621
	j_0	3.451	0.534	0.1	0.25	0.0	2.0	0.0		
^{208}Pb	Standard	6.631	0.658	0.0				0.0		
	Interior	6.631	0.658	0.0				0.3	1.0	0.0
	Surface	6.631	0.658	0.0				0.05	1.0	6.631
	Tail	6.631	0.658	0.0				0.01	1.0	8.077
	j_0	6.631	0.658	0.3	0.18	0.0	2.0	0.0		

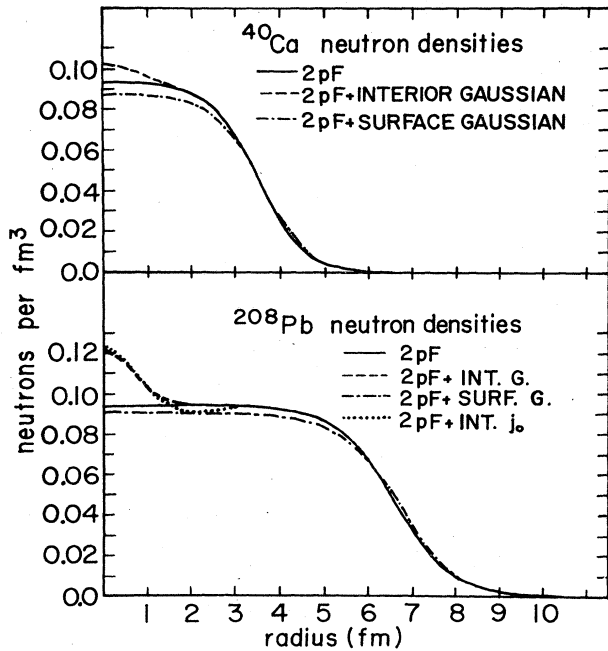


FIG. 6. Neutron model densities for ^{40}Ca and ^{208}Pb assumed in the sensitivity studies (see the text and Table I).

tively weak K^+A interaction. Consequently, meaningful sensitivity to the densities exists throughout the angular range depicted by the solid curves in Figs. 7–10 (except near the few indicated minima).

The results demonstrate that the calculated K^+A cross sections are, in general, about an order of magnitude more sensitive to interior density perturbations than are intermediate energy protons, provided the K^+ angular distributions extend to sufficiently large ($\sim 3 \text{ fm}^{-1}$) momentum transfer. This is evident for both the interior Gaussian bump and the damped $j_0(\omega r)$ perturbation. Note that the greatest sensitivity occurs in regions of large momentum transfer, $q \geq 2 \text{ fm}^{-1}$, which extends, for instance, significantly beyond the angular domain of the Marlow *et al.* data.²⁰ As expected, the pA cross sections show more sensitivity to the surface region²⁴ while both give comparable sensitivity to the tails of the density. These results may be compared with the estimates given in Refs. 8, 11, 21, 24, 38, and 39 of the large uncertainties in interior matter densities obtained in analyses of conventional hadron-nucleus elastic scattering data.

Typical variations between different theoretical models and empirical charge density distributions in the interior are of the order of 5–10% (Ref. 2). Based on the results displayed in Figs. 2–5 and 7–10, detection of interior neutron density fluctuations of this magnitude requires that the K^+A data extend to 3 fm^{-1} with 5% and 2–3% accuracy being needed for ^{40}Ca and ^{208}Pb targets, respec-

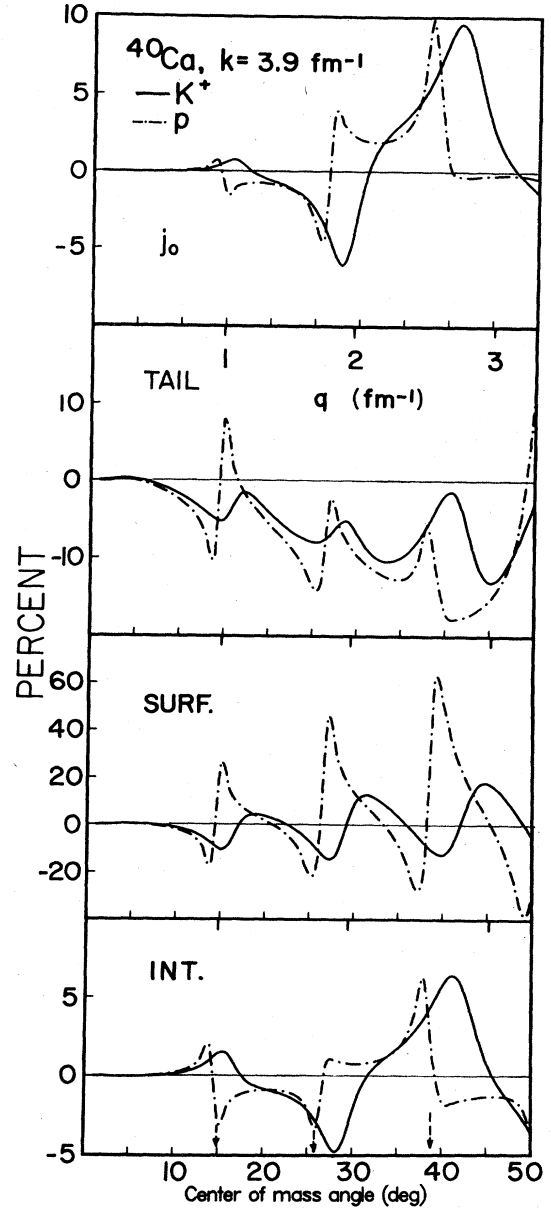


FIG. 7. Percent changes in the ^{40}Ca K^+A (solid curves) and pA (dot-dashed curves) lower energy elastic differential cross sections due to the perturbations in the neutron densities. Dashed arrows denote minima in the proton angular distributions.

tively. Of course, refinements to the reaction model such as medium corrections,¹² correlations,^{8,17} off-shell effects,^{35,36} relativistic dynamics corrections,¹⁴ etc., as well as better determined K^+N amplitudes, must be considered before more accurate densities can be deduced from analyses of K^+A data. The essential point to be drawn from the calculations presented here is that sufficient sensitivity of the K^+ meson to interior density fluctuations exists, and the type of new data necessary to provide new nuclear structure information has been specified explicitly.

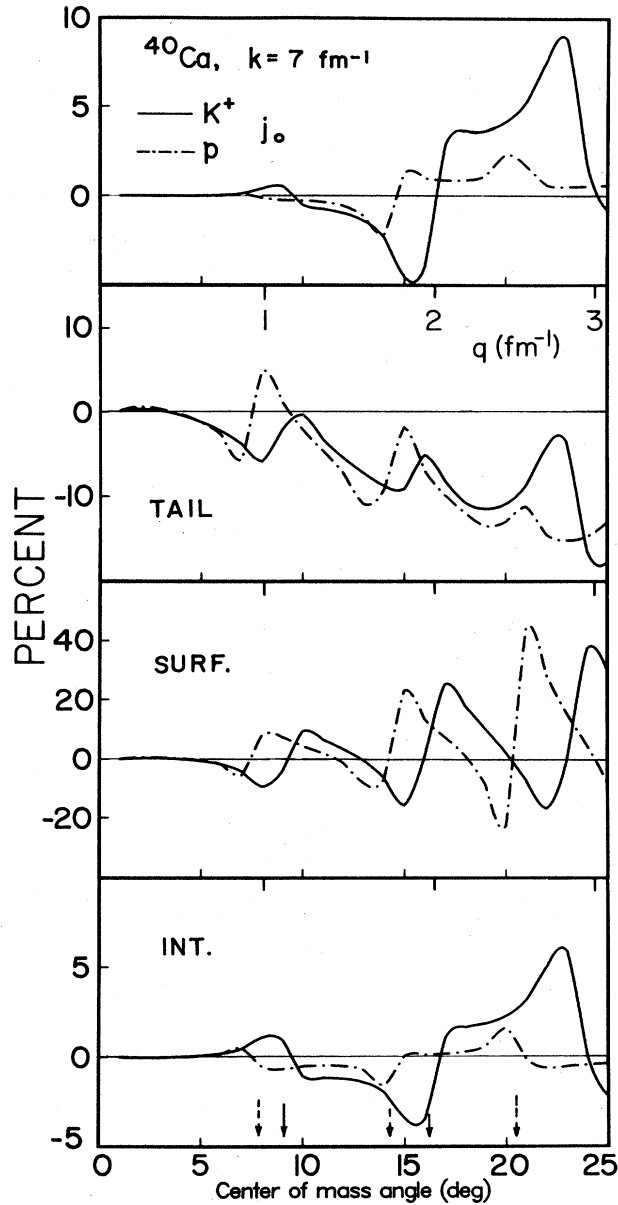


FIG. 8. Same as Fig. 7, except for ^{40}Ca at the higher energies. Solid arrows denote minima in the K^+ angular distributions.

IV. INELASTIC SCATTERING RESULTS

Inelastic scattering calculations for K^+ meson and proton induced transitions from ^{40}Ca and ^{208}Pb to the first excited 3^- states were also carried out at the same incident energies assumed in the elastic scattering analysis.

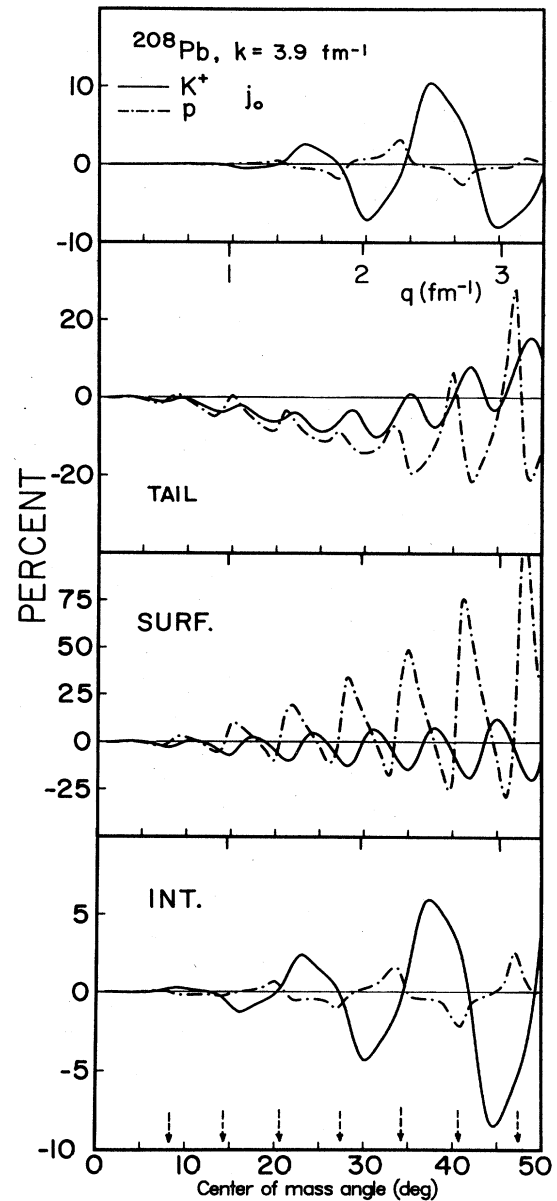


FIG. 9. Same as Fig. 7, except for ^{208}Pb at the lower energies.

The KMT-IA optical potential discussed in Sec. III, using the neutron model density of Eq. (11) with $A = s_1 = 0$, accounted for distortion of the incoming and outgoing projectile wave function. The DWBA formalism³¹ with a modified collective model transition potential given by³²

$$U_{\text{trans}}(r) = \frac{\beta_L}{\sqrt{2L+1}} \left[R \frac{d}{dr} U_{\text{opt}}(r) + (V + iW) e^{-[(r-c_0)/a_0]^2} \right] \quad (12)$$

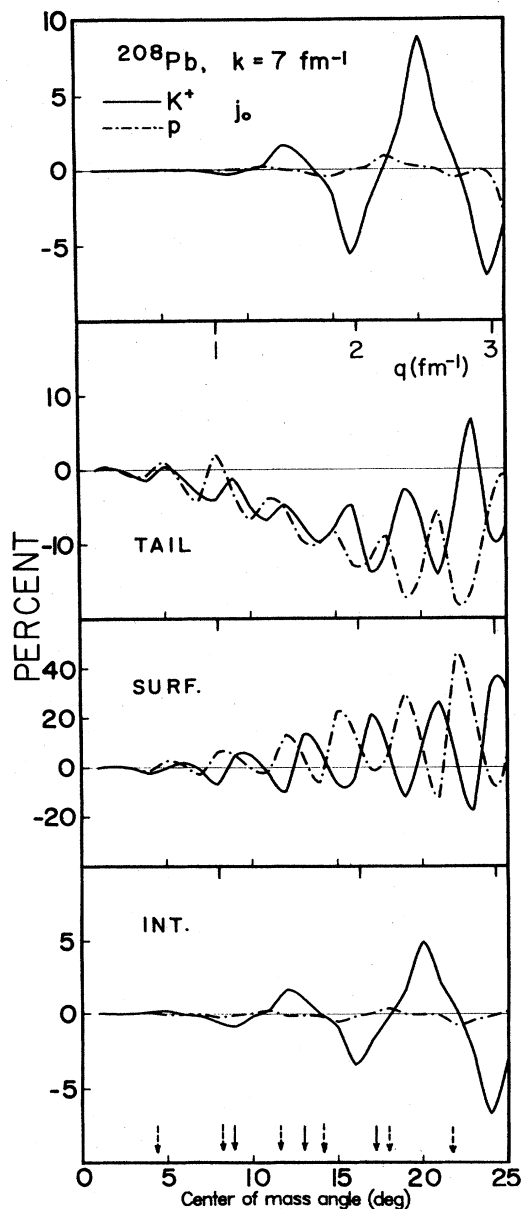


FIG. 10. Same as Fig. 7, except for ^{208}Pb at the higher energies.

was used to generate the theoretical inelastic angular distributions.

Two sets of calculations were carried out for K^+A and pA inelastic scattering at both energies. In the first set, $V=W=0$, thus providing reference inelastic cross sections. Each calculation was repeated with $a_0=1$ fm, c_0 equal to approximately one-half the nuclear half-density radius R , and V and W adjusted such that the height of the interior Gaussian bump was about 18% of the surface peak for both the real and imaginary parts of the transition potential. This procedure was intended to simulate the effects on the transition potential which would result from perturbations in the interiors of the underlying

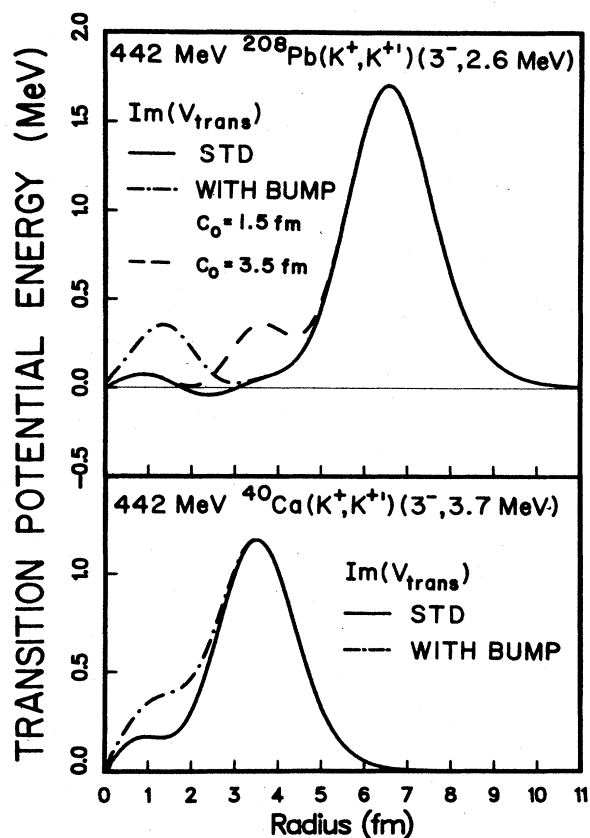


FIG. 11. Typical transition potentials for the (K^+, K^+) reaction for ^{40}Ca and ^{208}Pb targets showing the effect of the interior Gaussian perturbation.

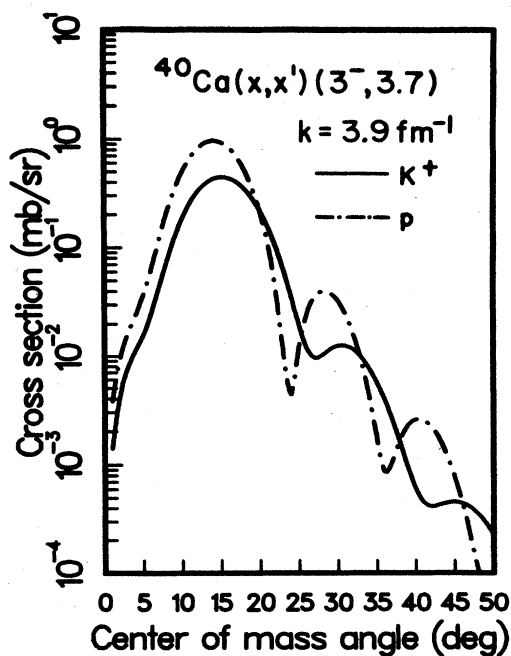
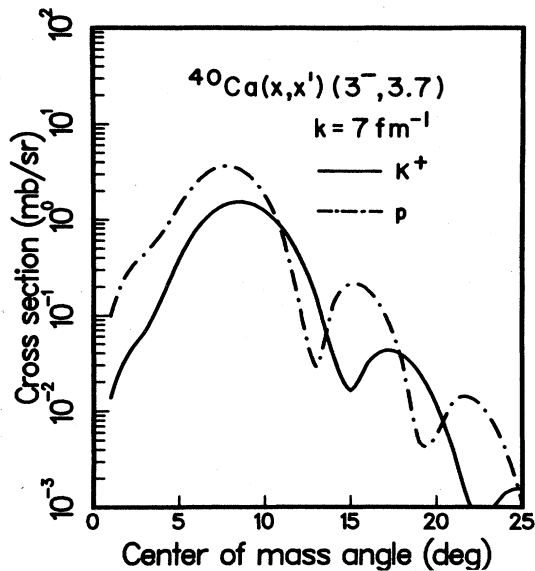
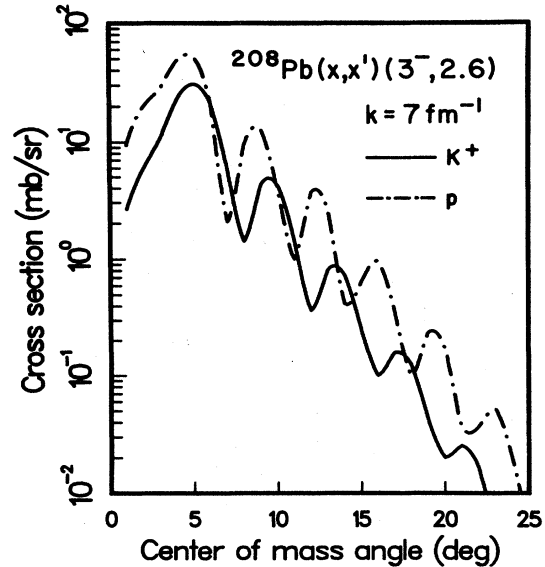
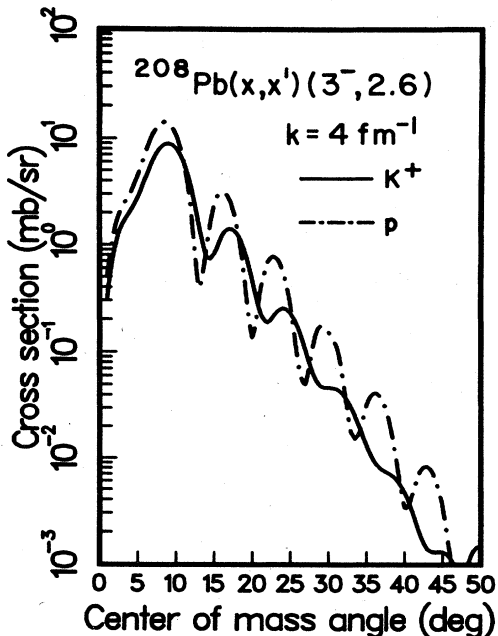


FIG. 12. DWBA predictions for the K^+ (solid curve) and proton (dot-dashed curve) inelastically induced transitions to the first 3^- state in ^{40}Ca at the lower incident energies.

TABLE II. Transition potential parameters.

Nucleus	Case	β_L	R (fm)	V (MeV)	W (MeV)	c_0 (fm)	a_0 (fm)
^{40}Ca	K^+ 442 MeV	0.1	3.42	-4.45	5.73	1.5	1.0
	K^+ 991 MeV	0.1	3.42	-3.52	8.46	1.5	1.0
	p 297 MeV	0.1	3.42	1.38	6.69	1.5	1.0
	p 800 MeV	0.1	3.42	-2.55	14.64	1.5	1.0
^{208}Pb	K^+ 442 MeV	0.1	5.925	-6.34	8.31	3.5	1.0
	K^+ 442 MeV	0.1	5.925	-6.34	8.31	1.5	1.0
	K^+ 991 MeV	0.1	5.925	-4.99	12.11	3.5	1.0
	p 297 MeV	0.1	5.925	1.962	11.25	3.5	1.0
	p 800 MeV	0.1	5.925	-4.17	22.84	3.5	1.0

FIG. 13. Same as Fig. 12, except for ^{40}Ca at the higher energies.FIG. 15. Same as Fig. 12, except for ^{208}Pb at the higher energies.FIG. 14. Same as Fig. 12, except for ^{208}Pb at the lower energies.

matter transition densities without actually carrying out the folding procedure.⁴⁰ This additional interior structure is comparable to that seen experimentally in the $^{208}\text{Pb}(3^-, 2.62 \text{ MeV})$ charge transition density.⁵ The overall coupling strength parameter β_L was arbitrarily taken to be 0.1 in all cases. For comparison, an additional calculation was made for $\text{K}^+ + ^{208}\text{Pb}$ at 442 MeV, in which the perturbation was placed even deeper within the nuclear interior. A complete list of the parameters used in the inelastic calculations is given in Table II.

Two typical transition potentials are shown in Fig. 11, both with and without the interior Gaussian perturbations. In addition, Fig. 11 displays the ^{208}Pb transition potential corresponding to two separate assumed values for c_0 . Note that only the nuclear interior region is affected by the Gaussian perturbations. A mixture of interior and surface fluctuations, as has been studied elsewhere,^{16,20} was not examined here.

The $^{40}\text{Ca}(x,x')(3^-, 3.74 \text{ MeV})$ and $^{208}\text{Pb}(x,x')(3^-, 2.62 \text{ MeV})$ (where x represents the K^+ meson or proton projectile) inelastic angular distributions corresponding to $V=W=0$ are shown in Figs. 12–15. Note that the (p,p') inelastic transitions are stronger and more diffractive than

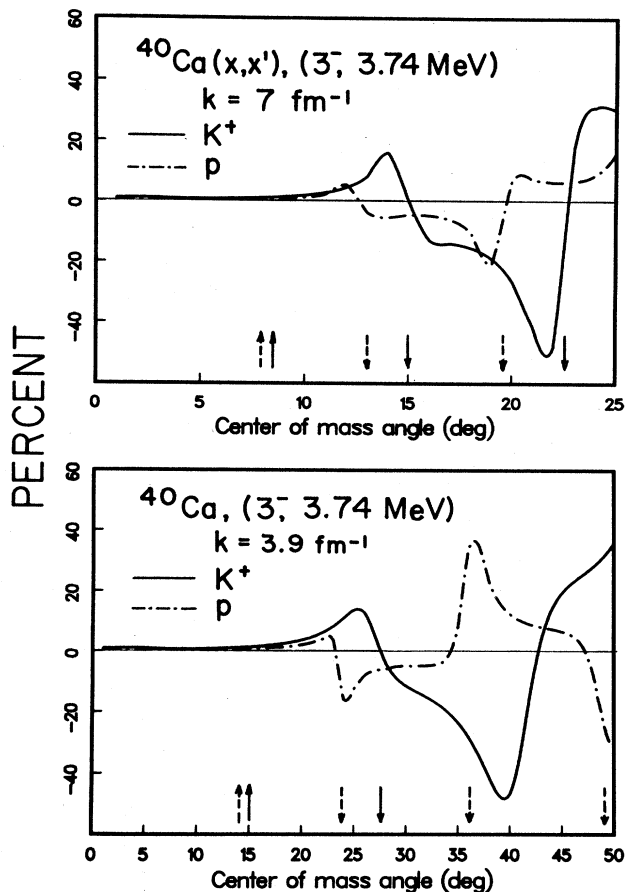


FIG. 16. Percent change in the K^+ (solid curves) and proton (dot-dashed curves) induced inelastic differential cross sections for ^{40}Ca resulting from the Gaussian bump in the interior of the transition potential. Arrow pointing up (down) denotes maxima (minima) in the angular distributions.

the (K^+, K^+) angular distributions as expected, owing to the much stronger central imaginary potential for the proton projectile.

The percent changes in the (x, x') angular distributions due to the interior modifications of the transition potentials are presented in Figs. 16 and 17. Again, enhanced sensitivity of the K^+ observables compared to that for intermediate energy protons is evident, particularly for ^{208}Pb . As in the case of elastic scattering, it is found that (K^+, K^+) data must extend to a momentum transfer of 3 fm^{-1} to achieve sufficient sensitivity to fluctuations in the interior transition density. Detection of 10% interior neutron transition density perturbations (relative to the surface peak strength), would require $^{40}\text{Ca}(K^+, K^+)$ data extending to 3 fm^{-1} with an overall accuracy of 10% or better. In the case of $^{208}\text{Pb}(K^+, K^+)$, data accurate to 2–3% extending to 3 fm^{-1} would be required in order to detect 10% interior density fluctuations. It is interesting to note, from Fig. 17, that shifting the perturbation further into the interior (i.e., from 3.5 to 1.5 fm) does *not* significantly alter the observed sensitivity of the (K^+, K^+)

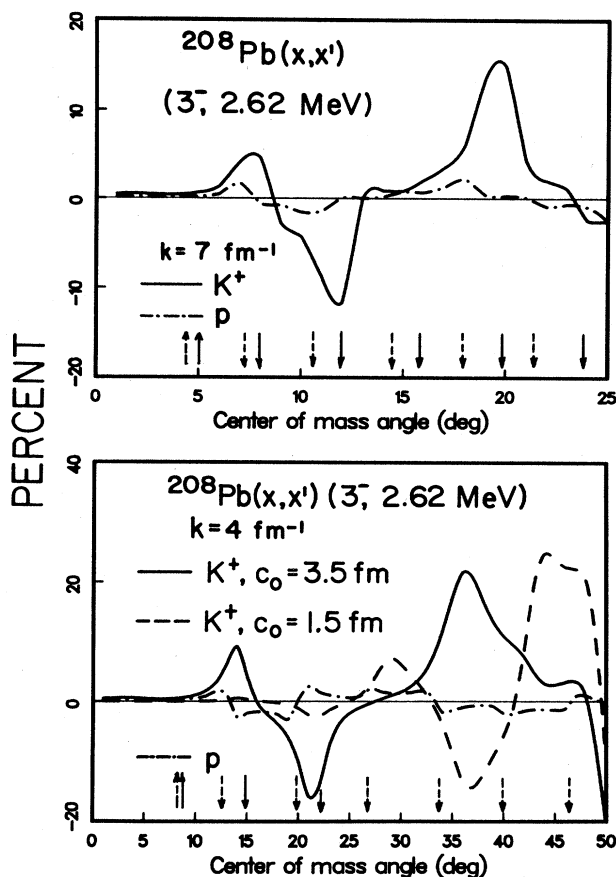


FIG. 17. Same as Fig. 16, except for ^{208}Pb . The dashed curve for the K^+A reaction corresponds to $c_0 = 1.5 \text{ fm}$.

angular distributions. This is encouraging since it indicates that observables at moderate momentum transfer remain sensitive to density fluctuations even near the centers of heavy nuclei.

V. SUMMARY AND CONCLUSIONS

In this work the $K^+ + ^{40}\text{Ca}$ and $K^+ + ^{208}\text{Pb}$ elastic and inelastic differential cross sections at 3.9 and 7 fm^{-1} c.m. momentum were calculated within the framework of the KMT formalism. Comparisons between the K^+A angular distributions and corresponding pA results at comparable incident momenta were made in order to determine the relative sensitivity of K^+A and pA observables to details of the underlying neutron ground state and transition density distributions in the nuclear interior.

These results demonstrate quantitatively that medium energy K^+A elastic and inelastic angular distributions are roughly an order of magnitude more sensitive to density fluctuations in the nuclear interior than are pA angular distributions. Our calculations also give an idea of the angular range and statistical quality of K^+A scattering data necessary to permit detection of interior density fluctuations of the order of 5–10%. The required momentum

transfer range of $0 \leq q \leq 3 \text{ fm}^{-1}$ is seen to extend well beyond the best available data.²⁰

This sensitivity study supports the expectation that K^+ mesons will provide a means for mapping out the interior nuclear matter distributions. We stress, however, that a much more precise understanding of the K^+A reaction process is essential before the extraction of interior density

information is possible. From the discussion in Sec. II it is clear that a satisfactory theoretical description of K^+A elastic scattering will not be as straightforward as had been previously thought. Vigorous efforts by both theorists and experimentalists will be required before new nuclear structure information can be gleaned from the study of K^+A scattering.

- ¹J. L. Friar and J. W. Negele, in *Advances in Nuclear Physics*, edited by M. Baranger and E. Vogt (Plenum, New York, 1975), Vol. 8, p. 219.
- ²B. Frois, in *Lecture Notes in Physics*, edited by J. Ehlers *et al.* (Springer, Berlin, 1979), Vol. 108, p. 52.
- ³I. Sick *et al.*, Phys. Lett. **88B**, 245 (1979).
- ⁴B. Frois *et al.*, Phys. Rev. Lett. **38**, 152 (1977).
- ⁵J. Heisenberg, J. Lichtenstadt, C. N. Papanicolas, and J. S. McCarthy, Phys. Rev. C **25**, 2292 (1982); J. Lichtenstadt, Ph.D. thesis, MIT, 1979 (unpublished); J. Heisenberg, private communication.
- ⁶H. D. Wohlfahrt, O. Schwentker, G. Fricke, H. G. Andresen, and E. B. Shera, Phys. Rev. C **22**, 264 (1980); H. D. Wohlfahrt, E. B. Shera, M.V. Hoehn, Y. Yamazaki, and R. M. Steffen, *ibid.* **23**, 533 (1981).
- ⁷J. L. Friar, in *The Interaction Between Medium Energy Nucleons in Nuclei—1982* (Indiana University), Proceedings of the Workshop on the Interaction Between Medium Energy Nucleons in Nuclei, AIP Conf. Proc. No. 97, edited by H. O. Meyer (AIP, New York, 1983), p. 378.
- ⁸L. Ray, Phys. Rev. C **19**, 1855 (1979).
- ⁹J. Hüfner, Phys. Rep. **21**, 1 (1975).
- ¹⁰A. W. Thomas and R. H. Landau, Phys. Rep. **58**, 121 (1980).
- ¹¹H. J. Gils, H. Rebel, and E. Friedman, Phys. Rev. C **29**, 1295 (1984).
- ¹²H. V. von Geramb, in *The Interaction Between Medium Energy Nucleons in Nuclei—1982* (Indiana University), Proceedings of the Workshop on the Interaction Between Medium Energy Nucleons in Nuclei, AIP Proc. No. 97, edited by H. O. Meyer (AIP, New York, 1983), p. 44; L. Rikus and H. V. von Geramb, Nucl. Phys. **A426**, 496 (1984).
- ¹³A. K. Kerman, H. McManus, and R. M. Thaler, Ann. Phys. (N.Y.) **8**, 551 (1959).
- ¹⁴J. A. McNeil, J. Shepard, and S. J. Wallace, Phys. Rev. Lett. **50**, 1439 (1983); J. Shepard, J. A. McNeil, and S. J. Wallace, *ibid.* **50**, 1443 (1983); B. C. Clark, S. Hama, R. L. Mercer, L. Ray, and B. D. Serot, *ibid.* **50**, 1644 (1983).
- ¹⁵C. B. Dover, and G. E. Walker, Phys. Rep. **89**, 1 (1982).
- ¹⁶S. R. Cotanch, Phys. Rev. C **23**, 807 (1981); **21**, 2115 (1980).
- ¹⁷A. Chaumeaux and M.-C. Lemaire, Phys. Rev. C **28**, 772 (1983).
- ¹⁸C. B. Dover and P. J. Moffa, Phys. Rev. C **16**, 1087 (1977).
- ¹⁹C. B. Dover, in *Low & Intermediate Energy Kaon-Nucleon Physics*, edited by E. Ferrari and G. Violini (Reidel, Boston, 1981), p. 165.
- ²⁰D. Marlow *et al.*, Phys. Rev. C **25**, 2619 (1982).
- ²¹W. R. Coker, G. W. Hoffmann, and L. Ray, Phys. Lett. **135B**, 363 (1984).
- ²²The pN phase shifts are taken from R. A. Arndt *et al.*, Phys. Rev. D **28**, 97 (1983) using the Virginia Polytechnic Institute (VPI) scattering analysis interactive dial-in (SAID) program. The K^+p phase shifts are also obtained from the VPI-SAID program solution CMK. The high partial wave K^+n phase shift solutions of K. Hashimoto, Phys. Rev. C **29**, 1377 (1984) were also used; these were obtained using the VPI-SAID program with solution HASH; and also K. Hashimoto, private communication.
- ²³L. Ray, see Ref. 7, p. 121.
- ²⁴L. Ray, W. R. Coker, and G. W. Hoffmann, Phys. Rev. C **18**, 2641 (1978).
- ²⁵B. R. Martin, Nucl. Phys. **B94**, 413 (1975).
- ²⁶B. R. Martin and C. G. Oades, in Proceedings of the IV International Conference on Baryon Resonances, Toronto, 1980; and private communication.
- ²⁷S. J. Watts *et al.*, see Ref. 19, p. 215.
- ²⁸L. Ray and W. R. Coker, Phys. Rev. C **24**, 1806 (1981).
- ²⁹It can be shown that the relation between $t(q)$ and $F(q)$ obtained by combining Eqs. (6) and (7) is numerically equivalent to a more complicated kinematic relation derived strictly from relativistic invariant quantities, for most cases of interest, including those considered in this work. The relativistic expression relating $t(q)$ and $F(q)$ is given for proton projectiles in L. Ray and G. W. Hoffmann, Phys. Rev. C **31**, 538 (1985). The generalization to meson projectiles is straightforward.
- ³⁰W. Bertozzi, J. Friar, J. Heisenberg, and J. W. Negele, Phys. Lett. **41B**, 408 (1972).
- ³¹G. R. Satchler, Nucl. Phys. **55**, 1 (1964).
- ³²T. Tamura, W. R. Coker, and F. Rybicki, Comp. Phys. Commun. **2**, 94 (1971).
- ³³L. Ray and W. R. Coker, Phys. Lett. **79B**, 182 (1978).
- ³⁴J. W. Negele and D. Vautherin, Phys. Rev. C **5**, 1472 (1972); the numerical results given here are from the DME code of Negele.
- ³⁵P. B. Siegel, W. B. Kaufmann, and W. R. Gibbs, Phys. Rev. C **30**, 1256 (1984).
- ³⁶H. Garcilazo and W. R. Gibbs, Nucl. Phys. **A356**, 284 (1981).
- ³⁷L. Ray, in *Proceedings of the Third LAMPF II Workshop*, edited by J. C. Allred, T. S. Bhatia, K. Ruminer, and B. Talley, Los Alamos National Laboratory Conference Report LA-9933-C, Vol. 1, p. 419.
- ³⁸L. Ray *et al.*, Phys. Rev. C **23**, 828 (1981).
- ³⁹G. W. Hoffmann *et al.*, Phys. Rev. C **21**, 1488 (1980); *ibid.* **24**, 541 (1981).
- ⁴⁰L. Ray and G. W. Hoffmann, Phys. Rev. C **27**, 2133 (1983).